

# A Universal Nearest-Neighbor Estimator for Intrinsic Dimensionality

Eng-Jon Ong<sup>1</sup>, Omer Bobrowski<sup>1</sup>, Gesine Reinert<sup>2</sup>, and Primož Skraba<sup>1</sup>

<sup>1</sup>School of Mathematical Sciences, Queen Mary University of London

<sup>2</sup>Department of Statistics, Oxford University

**Abstract**—Estimating the intrinsic dimensionality (ID) of data is a fundamental problem in machine learning and computer vision, providing insight into the true degrees of freedom underlying high-dimensional observations. Existing methods often rely on geometric or distributional assumptions and can significantly fail when these assumptions are violated. In this paper, we introduce a novel ID estimator based on nearest-neighbor distance ratios that involves simple calculations and achieves state-of-the-art results. Most importantly, we provide a theoretical analysis proving that our estimator is *universal*, namely, it converges to the true ID independently of the distribution generating the data. We present experimental results on benchmark manifolds and real-world datasets to demonstrate the performance of our estimator.

## I. INTRODUCTION

The *manifold hypothesis* [42] states that high-dimensional data is most often concentrated on or around a lower dimensional space. The dimension of this lower dimensional structure is referred to as the *intrinsic dimensionality* (ID) of the data, measuring the degrees of freedom, or the number of latent variables capturing the structure of the data. Estimating the intrinsic dimensionality of data is a pivotal task in data analysis and machine learning [3], [5], [16], computer vision [21], [36], [20], [32], materials science [33], [44], signal processing [10], [30], dynamical systems [22], [39], and other areas. Existing methods face significant challenges such as the curse of dimensionality, scale dependence, and sensitivity to the underlying distribution.

In this paper we present L2N2 – a new ID estimator based on the loglog (L2) values of the nearest-neighbor (N2) distance ratio. The key properties of L2N2 are: (a) it is computationally efficient, (b) it is supported by statistical theory proving that it converges to the true ID, regardless of what the data distribution is, and (c) it achieves, and even surpasses, state-of-the-art results.

### A. Related Work

Dimensionality estimation is an extensively studied problem; we refer the reader to the comprehensive surveys [9], [4] for more details. There are several approaches to ID estimation, each with their own strengths and limitations, and we will briefly mention a few here.

A classical approach is to estimate the asymptotic slope of a given statistic as a function of the sample size. Examples include the correlation dimension [22], the box-counting dimension [8], and the minimum-spanning-tree dimension [15].

A second approach is based on various projection methods, looking for the number of directions with largest variance. This includes PCA and local PCA [19], MDS [38], Isomap [41], diffusion maps [12], and more.

The approach most relevant to our work is based on the relationship between the nearest-neighbor distances. Levina and Bickel [29] proposed a maximum likelihood ID estimator using the nearest-neighbor distances. This method assumes that locally the points follow the distribution of a homogeneous Poisson point process. The TwoNN (Two Nearest-Neighbors) method, by Facco et al. [18], builds on similar principles, using the ratio of the first and second nearest-neighbor distances to obtain a computationally efficient estimator. The GriDE (Generalized Ratios ID Estimator) method, by Denti et al. [17], generalizes the TwoNN estimator using multiple nearest-neighbor distances. This estimator demonstrates improved stability and accuracy, particularly in noisy and heterogeneous data distributions. The DANCo (Dimensionality from Angle and Norm Concentration) method, by Ceruti et al. [11], includes additional information from the angles between nearest neighbors.

Recent work further refines nearest-neighbor and likelihood-based approaches. Qiu et al. [37] study the finite-sample underestimation bias of nearest-neighbor estimators and propose an explicit correction that improves empirical accuracy. From a representation-learning perspective, Kärkkäinen [27] introduces an additive autoencoder framework in which the intrinsic dimension is inferred from reconstruction behavior as the latent dimension varies. Likelihood-based methods have also been explored: Horvat et al. [23] estimate intrinsic dimensionality using normalizing flows, leveraging invertible generative models to analyze the effective dimensional structure of the data distribution, while Tempczyk [40] proposes LIDL, a local likelihood-based estimator that connects intrinsic dimension to small-scale density behavior.

### B. Context and Contributions

A key property for any dimensionality estimator is *scale invariance*, namely, rescaling the data should have no effect on the results. Aside from making it independent to the choice of measurement units, which is clearly desirable, we focus here on a much less obvious, yet very powerful, consequence. Under some additional conditions, scale invariance may lead to the property of *universality* [6], [7] – the limiting distribution

of the estimator is independent of the distribution of the data. Our L2N2 estimator was designed to take advantage of this phenomenon, providing excellent performance under very minimal assumptions on the data.

The contributions of the paper are:

- We derive L2N2 – a new method for estimating ID from ratios of nearest neighbor distances.
- We provide a rigorous theoretical analysis of L2N2, and give the precise relationship between the ID and the computed statistic. Most importantly, we show that the proven guarantees for L2N2 do not require knowing the distribution of the data, and that they apply to a vast class of input distributions with only mild assumptions.
- As the theoretical results are asymptotic, we provide a method to deal with finite sample effects. We show that L2N2 achieves, and even exceeds, the state-of-the-art performance on benchmarking datasets. We also apply L2N2 to real-world datasets, showing consistent results with commonly accepted dimensionalities.

Our proofs apply for data supported on  $C^1$  manifolds with bounded densities, which already encompass a broad class of practical models. We believe the mechanism driving universality is substantially more general and should extend to settings such as fractal measures and stratified spaces. However, showing this rigorously remains a direction for future work.

The rest of the paper is organized as follows. Section II introduces our new dimensionality-estimation method, L2N2. Section III presents the theoretical analysis supporting L2N2. Section IV outlines the experimental setup, and Section V discusses the results. Section VI offers a concluding discussion. Additional derivations and empirical results for the constants in our method are given in the Appendices.

## II. NN-RATIO BASED DIMENSIONALITY ESTIMATION

Our dimensionality estimator is based on the ratio of nearest-neighbor distances. Notably, L2N2 only requires mean-value estimates, avoiding the need for explicitly knowing the distribution of the nearest-neighbor ratio.

Suppose that a finite set  $\mathcal{X} \subset \mathbb{R}^D$  is sampled from a  $d$ -dimensional subspace, with  $d < D$ . Our goal is to estimate  $d$  from  $\mathcal{X}$ . For  $x \in \mathbb{R}^D$  and  $k \geq 1$ , we define the  $k^{\text{th}}$  nearest neighbor distance of  $x$  with respect to  $\mathcal{X}$  as:

$$R_k(x, \mathcal{X}) := \inf \{r > 0 : |B_r(x) \cap \mathcal{X} \setminus \{x\}| \geq k\},$$

where  $B_r(x)$  is the  $D$ -dimensional Euclidean ball of radius  $r$  around  $x$ . For  $k > j \geq 1$  we define,

$$L_{k,j}(x, \mathcal{X}) := -\log \log \left( \frac{R_k(x, \mathcal{X})}{R_j(x, \mathcal{X})} \right), \quad (\text{II.1})$$

and its average,

$$\bar{L}_{k,j}(\mathcal{X}) = \frac{1}{|\mathcal{X}|} \sum_{x \in \mathcal{X}} L_{k,j}(x, \mathcal{X}). \quad (\text{II.2})$$

Theorem III.1 below shows that asymptotically,  $\bar{L}_{k,j}$  linearly depends on  $\log(d)$  (see Remark 1 for more details). Consequently, our proposed L2N2 estimator for  $d$  based on the  $(k, j)$ -nearest neighbor distances is

$$\hat{d}_{k,j}(\mathcal{X}) = \exp(\alpha_{k,j} \bar{L}_{k,j}(\mathcal{X}) + \beta_{k,j}), \quad (\text{II.3})$$

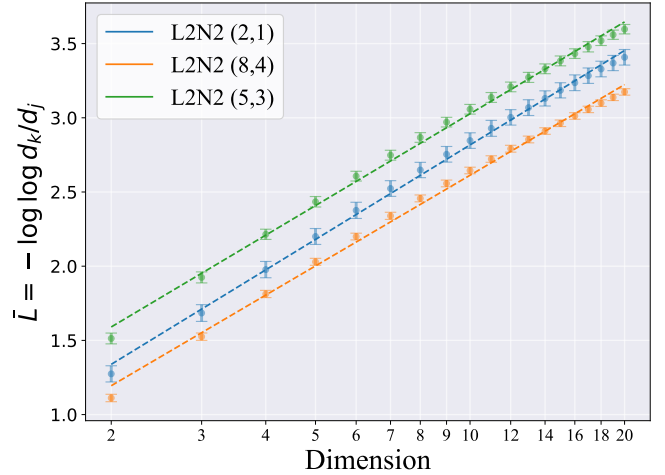


Fig. 1: The (approximately) linear relationship between  $\bar{L}_{k,j}$  and  $\log(d)$  (for  $(k, j) = (2, 1), (5, 3),$  and  $(8, 4)$ ). Here we used 2,500 points, sampled from the  $d$ -dimensional Gaussian distribution. The error bars are computed from 1000 independent trials.

where  $\alpha_{k,j}$  and  $\beta_{k,j}$  are pre-determined constants. Importantly, while  $\alpha_{k,j}$  and  $\beta_{k,j}$  might depend on the size of  $\mathcal{X}$ , they are otherwise *independent of any other property of the sample  $\mathcal{X}$  or its distribution*. This fact allows us to perform a simple tuning stage for our estimator, to optimize the values of  $\alpha_{k,j}$  and  $\beta_{k,j}$ . We use least-squares to fit the slope and intercept for  $\bar{L}_{k,j}(\mathcal{X})$  as a function of  $\log(d)$ , using samples generated by the  $d$ -dimensional normal distribution; see Fig. 1. We emphasize that the tuning stage is only performed once (for a given sample size), and the values of  $\alpha_{k,j}$  and  $\beta_{k,j}$  can be stored and reused in future applications, regardless of the type of the data (see supplementary materials for a table of precomputed values).

**Remark 1.** Theorem III.1 below states that asymptotically

$$\bar{L}_{k,j}(\mathcal{X}) \approx \log(d) + C_{k,j},$$

implying that we should take  $\alpha_{k,j} = 1, \beta_{k,j} = C_{k,j}$ . In practice, however, we observed that while this holds for a large sample size  $n$  (as the limit implies), for small sample sizes we have

$$L_{k,j}(\mathcal{X}) \approx \alpha_{k,j}^{(n)} \log(d) + \beta_{k,j}^{(n)},$$

where  $\alpha_{k,j}^{(n)} < 1$ . Therefore, to get the best results, we first need to learn the values of  $\alpha_{k,j}^{(n)}$  and  $\beta_{k,j}^{(n)}$ , suitable for the given sample size, as described above. The details on how we estimate these values are given in Section IV-A.

## III. THEORETICAL ANALYSIS

In this section we provide the theoretical analysis to support our estimator  $\hat{d}_{k,j}(\mathcal{X})$  (II.3), and to show that it is a consistent estimator for  $d$ , independently of the data distribution or its support. Let  $\mathcal{M} \subset \mathbb{R}^D$  be a  $d$ -dimensional  $C^1$  manifold

embedded in  $\mathbb{R}^D$ . We assume that  $f : \mathcal{M} \rightarrow \mathbb{R}$  is a probability density function on  $\mathcal{M}$ , such that

$$0 < f_{\min} = \inf_{\mathcal{M}} f \leq \sup_{\mathcal{M}} f = f_{\max} < \infty.$$

Let  $\mathcal{X}_n = \{X_1, \dots, X_n\}$  be a set of independent random variables with density  $f$ . We are interested in the limit of  $\bar{L}_{k,j}(\mathcal{X}_n)$  (II.2) as  $n \rightarrow \infty$ . We use  $Y_n \xrightarrow{P} Y$  to denote convergence in probability, i.e.  $\mathbb{P}(|Y_n - Y| \geq \epsilon) \rightarrow 0$  for any  $\epsilon > 0$  as  $n \rightarrow \infty$ .

**Theorem III.1.** *Under the assumptions above, as  $n \rightarrow \infty$ ,*

$$\bar{L}_{k,j}(\mathcal{X}_n) \xrightarrow{P} \log(d) + C_{k,j},$$

where  $C_{k,j}$  is independent of  $d$  and  $f$ , and is given in (III.4).

**Remark 2.** We make a few comments about Theorem III.1:

(1) The theorem shows a universal limit for the average  $L_{k,j}$  value, which is sufficient for justifying the use  $\hat{d}_{k,j}(\mathcal{X})$ . However, using the framework developed in [7], one can prove that, in fact, the *empirical distribution* of the collection of values  $\{L_{k,j}(X_i, \mathcal{X}_n)\}_{i=1, \dots, n}$  also admits a *universal limit*. Applications and a proof of this statement are left for future work.

(2) Theorem III.1 is limited to  $C^1$  manifolds. However, the space of  $C^1$  manifolds is quite general and covers many useful cases. Additionally, the good performance of the L2N2 estimator in practice suggests that the theorem holds in much greater generality. There are several significant challenges in generalizing the proofs to more general spaces, and so we will address this in future work.

(3) To prove Theorem III.1, we use the framework introduced in [35], for limit theorems of point processes on manifolds. It was originally used to show that the Levina-Bickel MLE estimator [29] is universal in the same sense as ours. As we show in Section V, while the MLE estimator also asymptotically converges to  $d$ , L2N2 performs significantly better in practice. We discuss this further in Section VI.

In the proof of Theorem III.1, we will make use of a truncated version of  $\bar{L}_{k,j}$ , ignoring points with a far-away  $k$ -nearest neighbor, making the estimator easier to control. For  $\mathcal{X}_n = \{X_1, \dots, X_n\}$ , we set

$$\bar{L}_{k,j,r}(\mathcal{X}_n) := \frac{1}{n} \sum_{i=1}^n L_{k,j,r}(X_i, \mathcal{X}_n),$$

where

$$L_{k,j,r}(x, \mathcal{X}_n) := L_{k,j}(x, \mathcal{X}_n) \cdot \mathbb{1}\{R_k(x, \mathcal{X}_n) \leq r\}, \quad (\text{III.1})$$

$\mathbb{1}\{\cdot\}$  is the indicator function, and  $r > 0$  is a constant. The proof of Theorem III.1 splits into three main parts:

**Step 1:** Show that the limit for the truncated average  $\bar{L}_{k,j,r}$  can be expressed by means of a mixture of homogeneous Poisson processes:

**Lemma III.2.** *For a fixed  $r > 0$ , as  $n \rightarrow \infty$ ,*

$$\bar{L}_{k,j,r}(\mathcal{X}_n) \xrightarrow{P} \int_{\mathcal{M}} \mathbb{E}\{L_{k,j}(\mathbf{0}, \mathcal{H}_{f(x)})\} f(x) dx,$$

where  $\mathcal{H}_\lambda$  is a homogeneous Poisson process in  $\mathbb{R}^d$  with rate  $\lambda$ , and  $\mathbf{0}$  is the origin in  $\mathbb{R}^d$ .

Intuitively, the integral in Lemma III.2 says that, in the limit, we have points covering the manifold  $\mathcal{M}$ , and the neighborhood of each point looks like a homogeneous Poisson process with rate  $f(x)$ .

**Step 2:** Show that the loss of the truncated version is negligible, so that  $\bar{L}_{k,j,r} \approx \bar{L}_{k,j}$ :

**Lemma III.3.**  $\lim_{n \rightarrow \infty} \mathbb{P}(\bar{L}_{k,j,r}(\mathcal{X}_n) \neq \bar{L}_{k,j}(\mathcal{X}_n)) = 0$ .

**Step 3:** Compute the expected value for a homogeneous Poisson process around the origin:

**Lemma III.4.** *Let  $\mathcal{H}_\lambda$  be a homogeneous Poisson process in  $\mathbb{R}^d$  with rate  $\lambda$ , then*

$$\mathbb{E}\{L_{k,j}(\mathbf{0}, \mathcal{H}_\lambda)\} = \log(d) + C_{k,j},$$

where  $C_{k,j}$  is given in (III.4), and is independent of  $d, \lambda$ .

The proof for Lemma III.4 reveals the connection between  $\bar{L}_{k,j}$  and the intrinsic dimension  $d$  and so is given below. The proofs for Lemmas III.2 and III.3 are more technical, mainly consisting of bounding moments. Using Lemmas III.2-III.4, we can now prove our main theorem.

## A. Proofs

*Proof of Theorem III.1.* Set,

$$L := \int_{\mathcal{M}} \mathbb{E}\{L_{k,j}(\mathbf{0}, \mathcal{H}_{f(x)})\} f(x) dx.$$

From Lemmas III.2 and III.3 we have that for any  $\epsilon > 0$ ,

$$\begin{aligned} \mathbb{P}(|\bar{L}_{k,j}(\mathcal{X}_n) - L| > \epsilon) &\leq \mathbb{P}(|\bar{L}_{k,j,r}(\mathcal{X}_n) - L| > \epsilon/2) \\ &\quad + \mathbb{P}(|\bar{L}_{k,j}(\mathcal{X}_n) - \bar{L}_{k,j,r}(\mathcal{X}_n)| > \epsilon/2) \rightarrow 0, \end{aligned}$$

hence  $\bar{L}_{k,j}(\mathcal{X}_n) \xrightarrow{P} L$ , as  $n \rightarrow \infty$ . From Lemma III.4 it follows that  $L = \log(d) + C_{k,j}$ .  $\square$

*Proof of Lemma III.2.* We will use Theorem 3.1 from [35], which proves the result for translation and rotation invariant functionals which satisfy a moment condition. From the definitions of  $L_{k,j}$  (II.1) and  $L_{k,j,r}$  (III.1), it is clear the  $L_{k,j}$  functional is both translation and rotation invariant, as required in [35]. So for Theorem 3.1 in [35] to hold we need to show that

$$\sup_n \mathbb{E}\{|L_{k,j,r}(X_1, \mathcal{X}_n)|^p\} < \infty,$$

for some  $p > 2$ . Conditioning on both  $X_1$  and  $R_k(X_1, \mathcal{X}_n)$ ,

$$\begin{aligned} \mathbb{E}\{|L_{k,j,r}(X_1, \mathcal{X}_n)|^p\} &= \int_0^\infty \mathbb{P}(|L_{k,j,r}(X_1, \mathcal{X}_n)|^p > t) dt \\ &= \int_0^\infty \int_{\mathcal{M}} \int_0^r \mathbb{P}\left(|L_{k,j}| > t^{1/p} \mid X_1 = x, R_k = u\right) \\ &\quad \times f_{R_k}(u|x) f(x) du dx dt, \end{aligned}$$

where  $L_{k,j} = L_{k,j}(X_1, \mathcal{X}_n)$ ,  $R_k = R_k(X_1, \mathcal{X}_n)$ , and  $f_{R_k}(u|x)$  is the conditional density of  $R_k$  given  $X_1 = x$ . Next, define

$$I_1(t, u) := \mathbb{P}\left(L_{k,j} < -t^{1/p} \mid X_1 = x, R_k = u\right)$$

$$I_2(t, u) := \mathbb{P}\left(L_{k,j} > t^{1/p} \mid X_1 = x, R_k = u\right).$$

We will bound each term separately. For  $I_1$ , note that  $L_{k,j} < -t^{1/p}$  is equivalent to  $R_k/R_j > v_1^{-1}$ , where  $v_1 = v_1(t) := e^{-e^{t^{1/p}}}$ . Therefore,

$$I_1(t, u) = \mathbb{P}(R_j < v_1 R_k \mid X_1 = x, R_k = u).$$

When  $R_k = u$ , we know that  $B_u(x)$  contains exactly  $(k-1)$  points from  $\mathcal{X}_{n-1}$ . In addition, if  $R_j < v_1 R_k$  then the ball  $B_{v_1 u}(x)$  contains at least  $j$  points out of these  $(k-1)$  points. Therefore, denoting  $F(A) = \int_A f(z) dz$ ,

$$I_1(t, u) \leq \binom{k-1}{j} \left( \frac{F(B_{v_1 u}(x))}{F(B_u(x))} \right)^j \leq C_1 v_1^{jd} < C_1 v_1,$$

where  $C_1 > 0$  is a constant that does not depend on  $x, t, u$ , and we used Lemma 4.3 in [35]. Since our bound is independent of  $u$  and  $x$ , we have

$$\int_0^\infty \int_{\mathcal{M}} \int_0^r I_1(t, u) f_{R_k(u)} f(x) du dx dt$$

$$\leq C_1 r \int_0^\infty e^{-e^{t^{1/p}}} dt. \quad (\text{III.2})$$

For  $I_2$ , note that  $L_{k,j} > t^{1/p}$  is equivalent to  $R_k/R_j < v_2^{-1}$  where  $v_2 = v_2(t) := e^{-e^{-t^{1/p}}}$ . Similarly to the above argument, we have that if  $R_j > v_2 R_k$  then at least  $(k-j)$  points in  $B_u(x) \setminus B_{v_2 u}(x)$ , and therefore,

$$I_2(t, u) \leq \binom{k-1}{k-j} \left( \frac{F(B_u(x)) - F(B_{v_2 u}(x))}{F(B_u(x))} \right)^{k-j}$$

$$\leq C_2 (1 - v_2^d)^{k-j} < C_2 (1 - v_2^d),$$

implying that

$$\int_0^\infty \int_{\mathcal{M}} \int_0^r I_2(t, u) f_{R_k(u)} f(x) du dx dt$$

$$\leq C_2 r \int_0^\infty (1 - e^{-e^{-t^{1/p}}}) dt. \quad (\text{III.3})$$

Since the right-hand-side on both (III.2) and (III.3) is finite for  $p = 3$ , the proof is complete.  $\square$

*Proof of Lemma III.3.* Note that if  $\bar{L}_{k,j,r} \neq \bar{L}_{k,j}$  then there exists  $i$  for which  $R_k(X_i, \mathcal{X}_n) > r$ . Therefore,

$$\mathbb{P}(\bar{L}_{k,j,r}(\mathcal{X}_n) \neq \bar{L}_{k,j}(\mathcal{X}_n)) \leq n \mathbb{P}(R_k(X_1, \mathcal{X}_n) > r)$$

$$= n \int_{\mathcal{M}} \mathbb{P}(R_k(X_1, \mathcal{X}_n) > r \mid X_1 = x) f(x) dx.$$

Given  $X_1 = x$ , let  $N_x$  be the number among the  $(n-1)$  points  $\{X_2, \dots, X_n\}$  which lie in  $B_r(x)$ . Then  $N_x \sim \text{Binomial}(n-1, F(B_r(x)))$ . Denote  $\mu_x = \mathbb{E}\{N_x\}$ . Note that from Lemma 4.3 in [35], we have

$$\mu_x = (n-1)F(B_r(x)) \geq C_\mu n r^d,$$

for some  $C_\mu > 0$ , independent of  $x$ . Applying a Chernoff-type bound for the binomial distribution (e.g., Lemma 1.1 in [34]), and assuming  $n$  sufficiently large so that  $\mu_x > 2(k-1)$ , then

$$\mathbb{P}(R_k(X_1, \mathcal{X}_n) > r \mid X_1 = x) = \mathbb{P}(N_x \leq k-1) \leq e^{-C\mu_x}.$$

Thus, we conclude that  $\mathbb{P}(\bar{L}_{k,j,r}(\mathcal{X}_n) \neq \bar{L}_{k,j}(\mathcal{X}_n)) \rightarrow 0$ , completing the proof.  $\square$

*Proof of Lemma III.4.* Denote  $R_k = R_k(\mathbf{0}, \mathcal{H}_\lambda)$ , and  $Y_k = \lambda \omega_d R_k^d$ , where  $\omega_d$  is the volume of a  $d$ -dimensional unit ball. Note that the sequence  $Y_1, Y_2, \dots$ , can be viewed as the arrival times of a unit-rate Poisson process, and therefore can be written as  $Y_k = \sum_{i=1}^k Z_i$ , where  $Z_1, Z_2, \dots$ , are independent with  $Z_i \sim \text{Exp}(1)$ . Fix  $1 \leq j < k$ , and set  $\Delta_{k,j} = Y_k - Y_j$ . Then  $Y_j \sim \text{Gamma}(j)$ , and  $\Delta_{k,j} \sim \text{Gamma}(k-j)$  are independent, and therefore,

$$U_{k,j} := \frac{Y_j}{Y_k} = \frac{Y_j}{Y_j + \Delta_{k,j}} \sim \text{Beta}(j, k-j).$$

Denoting  $L_{k,j} = L_{k,j}(\mathbf{0}, \mathcal{H}_\lambda)$ , then by (II.1),

$$L_{k,j} = \log \log \left( \left( \frac{Y_k}{Y_j} \right)^{1/d} \right) = \log(d) - \log \log(U_{k,j}^{-1})$$

Taking  $C_{k,j} = -\mathbb{E}\{\log \log(U_{k,j}^{-1})\}$ , then

$$C_{k,j} = - \binom{k-1}{j-1} \int_0^1 \log(-\log(u)) u^{j-1} (1-u)^{k-j-1} du$$

$$= - \binom{k-1}{j-1} \int_0^\infty \log(s) e^{-js} (1-e^{-s})^{k-j-1} ds$$

$$= - \binom{k-1}{j-1} \sum_{i=0}^{k-j-1} (-1)^i \binom{k-j-1}{i} \int_0^\infty \log(s) e^{-(i+j)s} ds,$$

$$= \binom{k-1}{j-1} \sum_{i=0}^{k-j-1} (-1)^i \binom{k-j-1}{i} \frac{\gamma + \log(i+j)}{i+j}. \quad (\text{III.4})$$

The last line follows from  $\int_0^\infty \log(s) e^{-(i+j)s} ds = \frac{-\gamma - \log(i+j)}{i+j}$ , where  $\gamma$  is the Euler-Mascheroni constant (see Appendix A for the calculation). As a special case, we have  $C_{2,1} = \gamma \approx 0.57721$ .  $\square$

#### IV. EXPERIMENTAL SETUP

In this section we provide the details for the experiments performed to evaluate the L2N2 estimator, and compare it against existing dimensionality estimation methods.

##### A. Tuning the L2N2 Estimator Parameters

We describe here the *parameter tuning stage* for the L2N2 estimator, where we optimize the values of  $\alpha_{k,j}$  and  $\beta_{k,j}$  in (II.3) to adjust for finite sample effects. We stress that the estimation is only needed to be carried out *once* for a given choice of  $(k, j)$  values and sample size  $n$ , and can be reused for any given dataset.

For each of choice of values of  $n$  and  $(k, j)$ , we generated 1,000 point clouds from a  $d$ -dimensional Gaussian distribution for various values of  $d$ . Using different distributions may affect the calculated parameter values. The Gaussian distribution

was chosen as it consistently yielded the best results across different settings. This approach can be conceived as equivalent to a grid-search method, and does not impose any prior distribution on the data. For each point-cloud, we computed the value of  $\bar{L}_{k,j}$  (II.2). Following the discussion in Section II, we use least-squares regression to find the best fit so that  $\bar{L}_{k,j} \approx \alpha_{k,j} \log(d) + \beta_{k,j}$ . We note that an important part of this tuning stage is the range of dimensions used to fit the values of  $\alpha_{k,j}, \beta_{k,j}$ . This stems from the fact that convergence rates become slower in higher dimensions. In practice, if there is an approximate range of candidate values, this can be used to improve accuracy. For example, for the benchmark experiments we used  $1 \leq d \leq 20$ , while for the real-world examples (except for ISOMAP), we used  $10 \leq d \leq 40$ .

### B. Evaluation Datasets

We tested the L2N2 estimator (II.3) on three datasets: (1) benchmark manifolds, proposed by Campadelli et al. [9], where the ground truth ID is known; (2) sampling from  $d$ -dimensional spheres with Gaussian noise; (3) real-world datasets with much higher ambient space dimensionalities, but with only conjectured ID’s.

1) *Benchmark Manifolds*: We evaluated L2N2 on a collection of synthetic datasets which is widely used in the ID literature [9], [18], [17], [4]. Each manifold has a known ID, embedding (ambient) dimension, and geometric/topological properties that make it suitable for benchmarking different estimators. The dataset consists of 24 different manifolds, with ID’s ranging from 1 to 70. The embedding dimensions are between 3 and 72. The geometry of these manifolds range from flat to various degrees of curvature. Table I gives the ambient dimension and underlying ID values for all the benchmark manifolds from [9] used in our experiments. We refer the reader to [9] for full details of the geometrical nature of these manifolds.

Name	Intrinsic dim. ( $d$ )	Ambient dim.
M1_Sphere	10	11
M2_Affine_3to5	3	5
M3_Nonlinear_4to6	4	6
M4_Nonlinear	4	8
M5a_Helix1d	1	3
M5b_Helix2d	2	3
M6_Nonlinear	6	36
M7_Roll	2	3
M8_Nonlinear	12	72
M9_Affine	20	20
M10a_Cubic	10	11
M10b_Cubic	17	18
M10c_Cubic	24	25
M10d_Cubic	70	71
M11_Moebius	2	3
M12_Norm	20	20
M13a_Scurve	2	3
M13b_Spiral	1	13
Mbeta	10	40
Mn1_Nonlinear	18	72
Mn2_Nonlinear	24	96
Mp1_Paraboloid	3	12
Mp2_Paraboloid	6	21
Mp3_Paraboloid	9	30

TABLE I: List of benchmark manifolds [9]

For testing the estimator performance, we use Mean Percentage Error (MPE) as the metric. Given an estimate  $\hat{d}$  and its corresponding ground truth  $d$ , the MPE is given by

$$\text{MPE} = 100 \times \frac{|\hat{d} - d|}{d}.$$

For each manifold, we evaluated the performance on point-clouds of 625, 1,250, 2,500 and 5,000 points, with 20 repetitions each. We compared L2N2 with 14 existing methods (see Table II). For methods with tuneable hyper-parameters, we used the values from [4], which optimize the average MPE across all manifolds. We evaluated the performance of  $\hat{d}_{k,j}$  for  $(k, j) = (2, 1), (4, 2), (8, 4)$ .

Finally, as a “sanity check”, in addition to the benchmark manifolds in [4], we tested L2N2 on 2,500 point samples from  $d$ -dimensional spheres, for  $10 \leq d \leq 40$ .

2) *Noisy Datasets*: In the original benchmark, the data lies completely on a low-dimensional manifold. Beyond the benchmark, we tested the effect of sampling noise (in the ambient space) on our estimator. We used the 6-dimensional sphere  $S^6$  embedded in  $\mathbb{R}^{11}$ , with point cloud of 2,500 points. We added mean zero Gaussian noise to each point, with standard deviations ( $\sigma$ ) of 0.01, 0.1 and 1.0. We performed 500 repetitions per  $\sigma$  value. We ran the same experiment for  $S^{10}$  embedded in  $\mathbb{R}^{11}$ . These experimental configurations allow us to compare against other methods using results from [4] (see supplementary materials).

3) *Real-World Datasets*: We evaluated L2N2 on the following real-world datasets: the ISOMAP face dataset [41], the MNIST dataset [28], the CIFAR-100 dataset [26] and the Isolet dataset [13].

The ISOMAP face dataset consists of 698 grayscale 64x64 images of a sculpture face obtained from different pose angles and lighting directions, so its ID is 3.

The MNIST dataset contains 70,000 grayscale images of 28x28 hand-written digits and its true ID is *not known*. However, as written digits are highly structured, the ID should be substantially smaller than 784.

The CIFAR-100 dataset [26] consists of 60,000 color images, each of resolution 32x32 pixels, resulting in a flattened vector of 3,072 dimensions.

Finally, the Isolet dataset [13] consists of features extracted from audio recordings of 150 subjects, pronouncing each letter of the alphabet twice, with 59 examples per speaker, totaling 7,797 examples with each example having 617 features.

To test the effect of sample size, we took 20 random subsets of the point clouds over a range of different subset sizes.

### C. Downstream Experiments

To further evaluate the accuracy of the L2N2 estimates, we conducted a downstream experiment using autoencoders on the MNIST dataset, where no ground truth is available. By testing different numbers of hidden units in the bottleneck layer, we checked for which choice the reconstruction error reaches an optimum, i.e. the smallest number of hidden units which result in a small error. The reasoning being that this should correspond to the intrinsic dimension. We used images corresponding to the individual digits. We created an autoencoder

No. Pts	625	1,250	2,500	5,000
L2N2(2,1)(r)	<b>8.52</b>	<b>6.97</b>	<b>6.06</b>	<b>5.52</b>
L2N2(2,1)(opt)	11.62	9.21	8.09	7.23
L2N2(2,1)	13.02	11.00	9.96	9.28
L2N2(4,2)	16.43	12.59	11.38	10.86
L2N2(8,4)	19.33	17.36	12.96	11.29
CDim [43]	53.91	50.81	45.78	43.83
CorrInt [22]	26.32	26.47	20.99	19.05
DANCo [11]	27.16	22.46	12.61	17.01
ESS [24]	23.34	16.95	17.15	14.88
FisherS [1]	40.92	42.09	42.24	42.26
GriDE [17]	13.86	11.89	10.98	10.12
kNN [14]	16.75	33.09	14.25	9.92
IPCA[19]	32.29	23.06	23.07	18.40
MIND ML[31]	13.36	12.90	20.43	20.28
MLE [29]	22.27	20.33	15.96	11.73
PH [5]	18.89	15.97	12.52	10.69
TLE [2]	24.44	22.69	20.57	14.65
TwoNN [18]	13.54	12.05	10.99	10.21
WODcap [25]	41.88	40.49	40.63	37.47

TABLE II: MPE for benchmark manifolds. The suffix “(r)” indicates that the estimated dimensions were rounded to the nearest integer, and “(opt)” indicates that the parameter values were optimized for the benchmark. Note the results reported for all methods other than L2N2 were optimized as well [4].

model that consisted of 6 layers with the following number of hidden units:  $256 \rightarrow 128 \rightarrow B \rightarrow 128 \rightarrow 256 \rightarrow 768$ , where  $B$  indicates the number of bottleneck hidden units. Mean squared error was used as the loss function for training and evaluation. The values of  $B$  were chosen in the range of 13 and 31, since it contains the intrinsic dimensionalities for different MNIST digits that the methods of TwoNN, GriDE, MLE and L2N2 converge to when all available data is used.

## V. EXPERIMENTAL RESULTS

In this section, we present the results for the different experiments: benchmark manifolds (Section V-A), noise experiments (Section V-B) and real-world datasets (Section V-C).

### A. Benchmark Manifold Results

The average MPE across all benchmark manifolds for all methods considered is shown in Table II. The MPE values for existing approaches from CDim to WODcap were obtained from [4]. It can be seen that L2N2(2,1), i.e.  $k = 2, j = 1$ , outperforms all other methods across all sample sizes. Note that all methods in Table II use parameters optimized for performance on the benchmark. We stress that for L2N2, *no such optimization was involved*, yet it yields better results. For a comparison on more equal terms, we also show the results for L2N2(2,1)(opt), where  $\alpha_{2,1}$  and  $\beta_{2,1}$  were optimized for the benchmark, yielding a substantial additional improvement. Finally, if we know the space has an integer dimension, we can further increase the accuracy by rounding the estimated dimensions (L2N2(2,1)(r)).

The next two methods with the best performance are the TwoNN and GriDE, which are of a similar nature to L2N2. A more detailed picture can be seen in the MPE scores across the individual benchmark manifolds, shown in Fig. 2(a). We observe that L2N2 performs better on non-linear manifolds, in particular when the ID is high. An exception to this is the

Method	$\sigma = 0.0$	$\sigma = 0.01$	$\sigma = 0.1$
L2N2(2,1)	6.10	6.16	8.48
IPCA	7.00	7.00	11.00
MLE	5.89	5.92	8.04
PH	5.94	5.97	8.21
KNN	6.00	5.97	9.17
WODCap	6.93	6.93	6.93
GRIDE	5.86	8.60	10.29
TwoNN	5.85	8.58	10.23
DANCo	6.92	8.95	11.00
MIND ML	6.00	9.00	10.00
CorrInt	5.82	7.48	9.00
ESS	6.07	7.87	10.36
FisherS	6.98	5.63	5.82
TLE	6.28	7.83	9.74

TABLE III: Average estimated dimensions for the noise experiments where  $S^6$  is embedded into  $\mathbb{R}^{11}$  with mean zero, variance  $\sigma^2$  Gaussian noise (in ambient space dimension) added.

M8\_nonlinear dataset. When we do not round our estimated dimensions, other methods are better when the ID is very low, such as  $d = 1$  or  $d = 2$ . Here, slight deviations from the ground truth can produce large MPEs (e.g., an estimate of  $\hat{d} = 1.1$  when  $d = 1$  gives an MPE of 10). However, rounding small dimensions almost always reveals the correct dimension, see Fig. 2(b). This explains the significant improvements obtained when we use dimension rounding.

The results for  $d$ -dimensional spheres are presented in Fig. 3. We see that L2N2 accurately recovers the true dimensionality of the spheres, whereas TwoNN, GriDE and MLE yield systematically lower estimates, with the gap increasing with the dimensions.

### B. Noise Experimental Results

Table III and IV presents the full results for the noise experiments for other dimensionality estimation approaches. It appears that all methods are sensitive to noise, and L2N2 performs competitively with the best of them. In both cases, the estimated dimensions increase with the amount of noise, as expected. The increase in L2N2 is comparable to the other methods. Generally, estimating the ID from noisy data is extremely challenging, and to some extent an ill-defined problem, as the dimension of the support of the distribution is the same as the ambient space. We leave it as future work to see if we can improve our estimates from noisy data.

### C. Real-World Dataset Results

The results for the ISOMAP dataset are in Fig. 4(a), comparing L2N2 with TwoNN, and GriDE. We can see that as the sample size increases, the predicted dimensionality of both methods approach the commonly accepted ground truth of 3. When all points are used, the L2N2 estimate is closer to 3, compared to the others.

The results for the MNIST datasets for the digit “1” are in Fig. 4(c). We find that L2N2 estimates are higher than the others. However, the changes in the estimates as the number of points varies follow a similar trend across both methods. Other digits behave similarly and can be found in the supplementary materials.

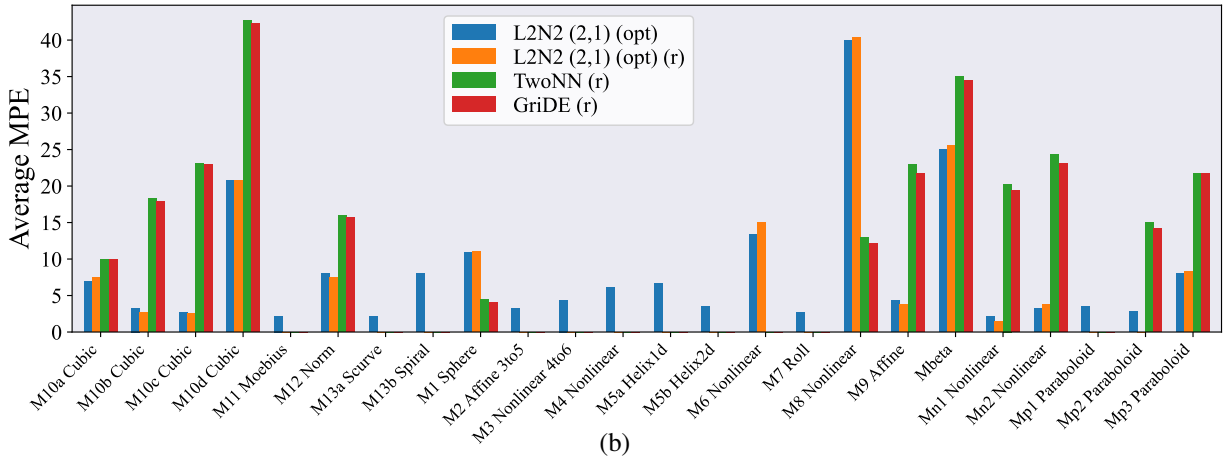
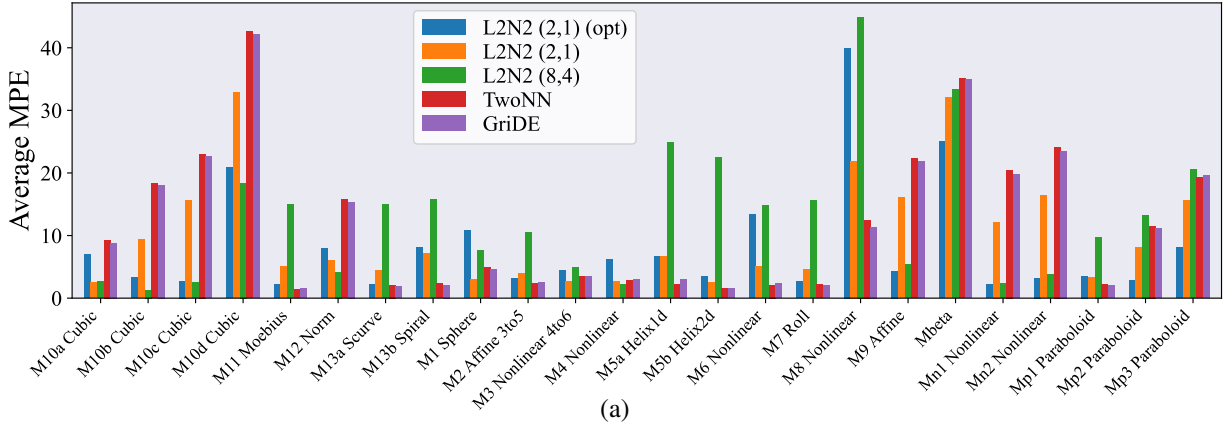


Fig. 2: (a) MPE scores of L2N2 with  $(k, j) = (2, j)$  and  $(8, 4)$ , TwoNN, and GriDE across the individual benchmark manifolds for 2,500 points. (b) Comparing the MPE when dimensionality rounding is used. L2N2 without rounding is here added for reference.

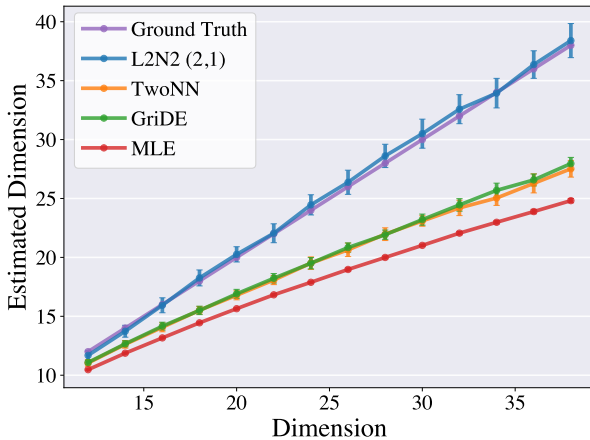


Fig. 3: Comparison of estimated ID of  $d$ -dimensional spheres for different methods and dimensions with the ground truth shown.

The results for the CIFAR-100 dataset is shown in Fig. 4(d). As with MNIST, our estimates are higher than those from other methods.

For the Isolet dataset, the results are in Fig. 4(b). We observe

Method	$\sigma : 0.0$	$\sigma : 0.01$	$\sigma : 0.1$
L2N2(2,1)	10.05	10.02	10.47
IPCA	11.00	11.00	11.00
MLE	9.26	9.25	9.61
PH	9.38	9.34	9.78
KNN	9.91	9.99	10.29
WODCap	9.15	9.15	9.15
GRIDE	9.40	9.77	10.48
TwoNN	9.40	9.82	10.51
MiND ML	9.40	10.00	10.00
CorrInt	9.10	9.32	9.22
ESS	10.00	10.27	10.65
FisherS	11.00	7.87	5.82
DANCo	10.90	11.00	11.00
TLE	10.10	9.89	10.02

TABLE IV: Average estimated dimensions for the noise experiments where  $S^{10}$  is embedded into  $\mathbb{R}^{11}$  with mean zero, variance  $\sigma^2$  Gaussian noise (in ambient space dimension) added.

that as the number of points increases, the estimated dimensionality decreases, with similar values for L2N2, TwoNN, and GriDE (between 10-12).

We note that for the MNIST, CIFAR-100, and Isolet datasets, the ID estimates produced by L2N2 are consistently higher than those obtained from TwoNN and GriDE. However,

it is known that these methods tend to underestimate intrinsic dimensionality, especially for higher dimensions. This is clearly illustrated in Fig. 3, where L2N2 accurately recovers the correct dimension, while TwoNN and GriDE yield systematically lower estimates.

#### D. Downstream Experiments Results

The results can be seen in Fig. 5. The ID estimated by TwoNN had reconstruction errors (average 0.0143) approximately 21% higher than those obtained with L2N2 (average 0.0119). Moreover, increasing the bottleneck beyond the L2N2 estimate does not improve performance any further, providing strong evidence that L2N2 estimates are quite accurate.

## VI. DISCUSSION

In this section we provide a few further insights about L2N2 and the results presented above.

**Nearest-Neighbor Configurations:** An important observation from the benchmark results is that the simplest ratio configuration  $(k, j) = (2, 1)$  consistently gives the best results (here we presented  $(4, 2)$  and  $(8, 4)$ , and see the supplementary materials for more examples). An explanation for this can be seen in Fig. 2(a). We find that using ratios from more distant neighbors negatively impacts the MPE for low dimensional manifolds such as the one-dimensional helix. This is likely due to the low number of points available (2,500), causing the 8-th nearest neighbor to lie on another part of the helix, and thus skewing the estimated dimensionality. In future work, we plan to explore in what cases, if any, other choices for  $(k, j)$  are preferable.

**Finite Sample Effects:** Lemma III.4 shows that the estimator is asymptotically unbiased at the log-scale. Finite-sample deviations arise because the analysis relies on the local homogeneity of the point process in the limit, which is rarely met in the finite setting. A theoretical analysis of the finite-sample bias remains as future work. Nevertheless, our experiments show that L2N2 exhibits much lower bias than competing methods (Fig. 3). More details and results of the effect of samples sizes on the coefficient estimates  $(\alpha_{i,k} \text{ \& } \beta_{i,k})$  can be found in Appendix C .

**Subsampling for Scaling:** For very large samples, we propose the following efficient strategy. We replace (II.2) with the average value of  $L_{k,j}$  taken over a small query subset. Note that the individual  $L_{k,j}$  values are still computed with respect to the full dataset. The results when subsampling is used on the benchmark manifold experiments can be found in Table V. It can be seen that subsampling in this manner increased the MPE by around 0.34%-0.56%, but with significant reduction in computational complexity. For comparison, when only 2,500 points are available in total, the MPE increases to 9.96%. However, in this case, this computational optimization is unnecessary.

**Comparison with the MLE:** Earlier in the paper, we mentioned that the MLE (Levina-Bickel estimator) has similar properties to the L2N2, including that it universally converges

No. Pts ( $\times 10^3$ )	15	50	100	500
(SubSamp) MPE	8.50	7.67	7.61	6.88
(Full Set) MPE	8.15	7.33	7.05	6.41
MPE Diff.	0.45	0.34	0.56	0.47

TABLE V: Benchmark manifold MPE from the subsampling experiments (no rounding or optimization). (Full Set) indicates that all points are used. (SubSamp) indicates that a random subset of 2,500 points are used.

to  $d$  [35]. However, the MLE performs significantly worse than L2N2 in practice. The MLE results from [4] where nearest neighbor values of  $k = 10, 20, 40$  and  $80$  were tried. It was consistently found that  $k = 10$  yielded the best results for the MLE, which are the ones used in Table II; larger  $k$  did not yield better results. Below we give a possible intuitive explanation for the gap in performance.

Consider the special case ( $k = 2$ ) of the MLE, given by

$$\hat{d}_{\text{MLE}}(\mathcal{X}_n) = \frac{1}{n} \sum_{i=1}^n \frac{1}{\log(R_2(X_i, \mathcal{X}_n)/R_1(X_i, \mathcal{X}_n))}.$$

Thus, we can write both estimators as an average

$$\frac{1}{n} \sum_{i=1}^n g(\log(R_2(X_i, \mathcal{X}_n)/R_1(X_i, \mathcal{X}_n))),$$

where for the MLE estimator we take  $g(x) = 1/x$ , while for the L2N2 we take  $g(x) = \log(1/x)$ . We suggest that the inferior performance of the MLE stems from the dynamic range of  $1/x$ , which explodes for small  $x$  and vanishes for large  $x$ . By contrast,  $\log(1/x)$  spreads mass more evenly across  $\mathbb{R}$ , suppressing both extremes.

**Runtime Complexity:** All the experiments in this paper were carried out on the CPU of the same Dell Desktop (Dell tower EBT2250, Intel Ultra 7, 16GB RAM). The main computational cost is the k-NN calculation (as in MLE, TwoNN, GriDE). Computing the mean loglog-ratio scales linearly with the sample size, with minimal memory overhead. In practice, L2N2 is consistently faster due to its simple mean-based estimate. On benchmark manifolds, average runtime is 13/23/56 ms for 2.5k/5k/10k points, compared to TwoNN 76/303/1243 and MLE 23/53/139.

**Future Work:** While L2N2 provides generally accurate estimates, the experiments do show significant effects from small sample sizes particularly in high intrinsic dimensions. In the future, we plan to investigate more principled approaches to improve accuracy on small samples. One such direction is to consider the entire distribution of  $\bar{L}_{k,j}$  rather than its mean value. We believe it is possible to prove that the limiting distribution is universal, and to find exactly what this distribution is. Another approach will be to devise a more systematic way to tune the parameters  $\alpha_{k,j}, \beta_{k,j}$ , that will take the sample size and the different ID ranges into account. Finally, we also plan to investigate the properties of the L2N2 estimator for different values of  $(k, j)$  in order to better understand in what cases can we benefit from using indexes other than  $(2, 1)$ .

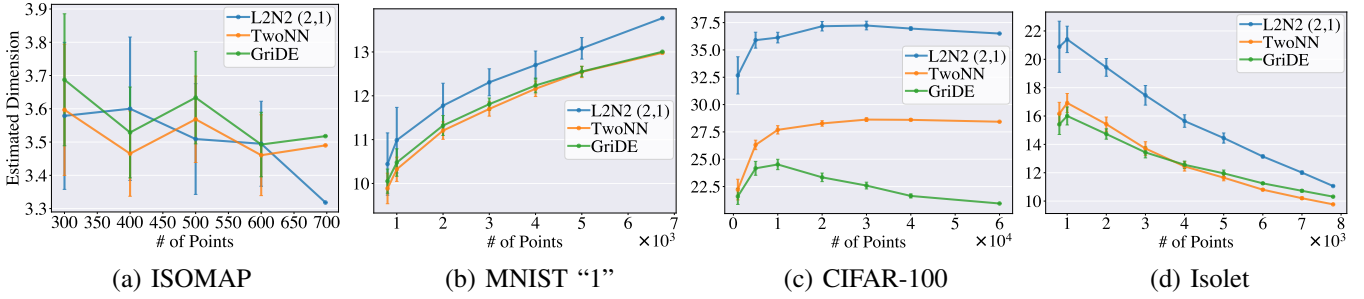


Fig. 4: Estimated ID for real datasets. (a) ISOMAP faces; (b) digit “1” in MNIST (other digits can be found in the supplemental material); (c) CIFAR-100; (d) Isolet dataset. Bars denote  $\pm 1$  standard deviation.

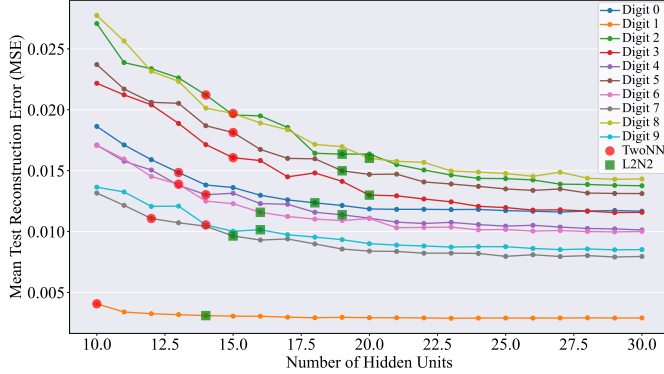


Fig. 5: Downstream experiments results: Reconstruction errors (MSE) of autoencoders with bottleneck layers set to different values.

#### APPENDIX A EVALUATING THE INTEGRAL IN $C_{k,j}$

In this section, we derive the last step for obtaining (3.2) by showing the following:

$$\int_0^\infty \log(s) e^{-(i+j)s} ds = \frac{-\gamma - \log(i+j)}{i+j} \quad (\text{A.1})$$

where  $\gamma \approx 0.5772$  is the Euler–Mascheroni constant and  $\log$  is the natural logarithm. This uses the Leibniz integral rule (also known as “differentiating under the integral”). Let  $\phi = i + j$  and define

$$I(z, \phi) = \int_0^\infty s^{z-1} e^{-\phi s} ds$$

$$[u = \phi s \Rightarrow] = \phi^{-z} \int_0^\infty u^{z-1} e^{-u} du = \phi^{-z} \Gamma(z),$$

where  $\Gamma$  is the Gamma function. Taking the partial derivative with respect to  $z$ , on one side we obtain

$$\frac{\partial I(z, \phi)}{\partial z} = \frac{\partial}{\partial z} (\phi^{-z} \Gamma(z))$$

$$= \phi^{-z} \frac{\partial \Gamma(z)}{\partial z} - \phi^{-z} \Gamma(z) \log(\phi).$$

On the other side, we obtain

$$\frac{\partial I(z, \phi)}{\partial z} = \int_0^\infty \frac{\partial}{\partial z} (s^{z-1} e^{-\phi s}) ds$$

$$= \int_0^\infty s^{z-1} \log(s) e^{-\phi s} ds.$$

Setting  $z = 1$  and equating the two, we obtain

$$\int_0^\infty \log(s) e^{-\phi s} ds = \phi^{-1} \left( \left. \frac{\partial \Gamma(z)}{\partial z} \right|_{z=1} - \Gamma(1) \log(\phi) \right)$$

$$= \frac{-\gamma - \log \phi}{\phi},$$

as  $\frac{\partial \Gamma(z)}{\partial z}$  evaluated at 1 is the negative of the Euler–Mascheroni constant, i.e.  $-\gamma$  and  $\Gamma(1)$  is 1. Substituting in  $\phi = i + j$  gives the result as required.

Finally, we use (A.1) in (3.2) to obtain

$$C_{k,j} = \binom{k-1}{j-1} \sum_{i=0}^{k-j-1} (-1)^i \binom{k-j-1}{i} \left( \frac{\gamma + \log(i+j)}{i+j} \right).$$

We observe that for  $k = 2, j = 1$ , the sum simplifies and we obtain  $C_{2,1} = \gamma$ . More generally, if  $k = j + 1$  then  $C_{k,j} = \gamma + \log(j)$ . A few other values of  $C_{k,j}$  for different values of  $k, j$  are given in the following table:

$k$	$j$	$C_{k,j}$
2	1	0.57722
3	1	-0.05796
5	1	-0.14338
5	2	0.03536
6	3	0.14185
8	4	0.10242
8	7	2.52310
10	8	0.85720

#### APPENDIX B ADDITIONAL MNIST EXPERIMENTAL RESULTS

The results for the digits “2”, “3” and “4” of the MNIST dataset can be found in Fig. 6. We find results that are consistent with Digit “1” in the main paper, where our predicted ID values are consistently higher than those of TwoNN and GriDE. We note that the gap between our predictions and TwoNN, GriDE is consistent with that shown in Fig. 3 of the main paper, suggesting a possible underprediction of ID by TwoNN and GriDE.

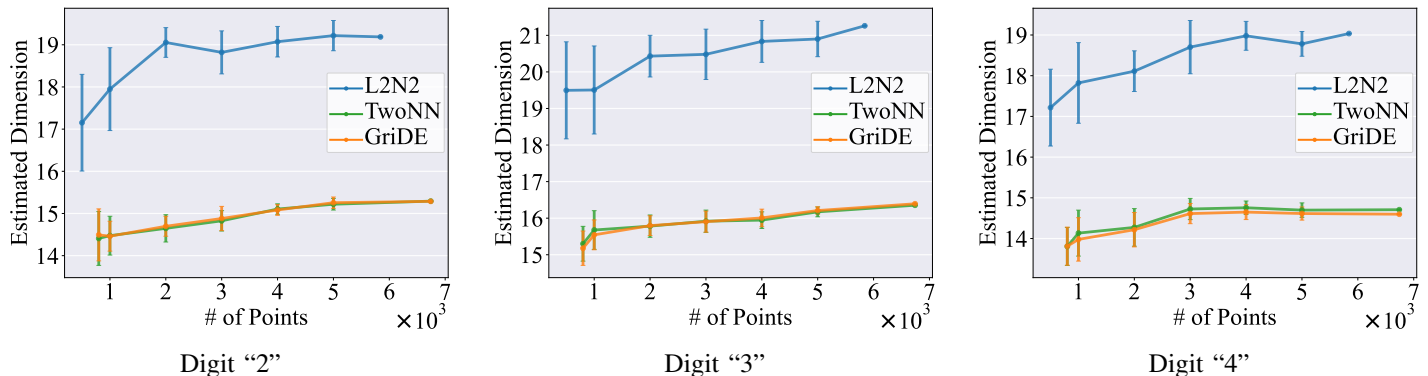


Fig. 6: Results for digits “2”, “3”, and “4” from the MNIST dataset. The error bars represent the standard deviation.

### APPENDIX C EMPIRICAL VALUES FOR $\alpha_{2,1}^{(n)}$ AND $\beta_{2,1}^{(n)}$

In this section, we provide more insight into the estimated values of  $\alpha_{2,1}^{(n)}$  and  $\beta_{2,1}^{(n)}$ . We show how the number of points  $n$ , the choice of dimensions used in the estimation, and the models used affect the estimated values. For each value, we generated 50 point clouds for a range of dimensions and used estimated the parameters using linear regression.

In Table VI, we show the estimated values for the  $d$ -dimensional Gaussian for  $n$  ranging from 100 to 500,000. The values were estimated using dimensions ranging from 1 to 20 as in the benchmark experiments. For samples larger than 2,500 points, we estimate the mean by computing the average of the log log of the nearest neighbor ratios of 2,500 randomly chosen points (with distances computed with the all the points). For 500,000 points, the values of  $\alpha_{2,1}^{(n)}$  and  $\beta_{2,1}^{(n)}$  are close to the theoretical values of 1 and  $\gamma = 0.57721$ , respectively. We also show the estimated parameters when the range of dimensions used was 10–40 in Table VII. In this case, the values are significantly different from the theoretical values but we do see  $\alpha_{2,1}^{(n)}$  slowly increasing toward 1 and  $\beta_{2,1}^{(n)}$  decreasing. This indicates that the convergence rate is slower in higher dimensions. While this is not surprising, as the experiments show, one method of mitigating these effects is to estimate the values using an approximate range of dimensions. This can also be seen clearly in Fig. 7, where we plot the estimated values for using different dimension ranges for the  $d$ -dimensional Gaussian. While all the values are converging, it is significantly slower if we include higher dimensions. The error bars represent the standard deviation.

Finally, we illustrate the effect of different sampling models in Fig. 8 and 9. In both cases the trend toward the theoretical values is clear, but in Fig. 8 for 1000 points and up, the Gaussian seems to converge faster.

### REFERENCES

- [1] Luca Albergante, Jonathan Bac, and Andrei Yu. Zinovyev. Estimating the effective dimension of large biological datasets using fisher separability analysis. *2019 International Joint Conference on Neural Networks (IJCNN)*, pages 1–8, 2019. 6
- [2] Laurent Amsaleg, Oussama Chelly, Michael E. Houle, Ken ichi Kawarabayashi, Miloš Radovanović, and Weeris Treeratanajaru. *Intrinsic Dimensionality Estimation within Tight Localities*, pages 181–189. 6

TABLE VI:  $d$ -dimensional Gaussian: Dimensions 1–20 used

# pts	$\alpha_{2,1}^{(n)}$	$\beta_{2,1}^{(n)}$
100	0.843130 ± 0.030100	0.774468 ± 0.063900
250	0.880452 ± 0.024624	0.730182 ± 0.052274
500	0.904643 ± 0.028951	0.703754 ± 0.061459
750	0.908416 ± 0.023954	0.702147 ± 0.050852
1,000	0.911129 ± 0.025758	0.703216 ± 0.054681
2,000	0.928568 ± 0.021527	0.675884 ± 0.045700
2,500	0.929932 ± 0.022381	0.675130 ± 0.047513
5,000	0.939984 ± 0.019841	0.666099 ± 0.042119
10,000	0.947112 ± 0.019408	0.656437 ± 0.041201
25,000	0.961028 ± 0.016408	0.633636 ± 0.034833
50,000	0.965780 ± 0.015902	0.631085 ± 0.033758
100,000	0.969699 ± 0.012250	0.621590 ± 0.026005
250,000	0.977754 ± 0.011862	0.610773 ± 0.025181
500,000	0.977408 ± 0.010183	0.613801 ± 0.021617

TABLE VII:  $d$ -dimensional Gaussian: Dimensions 10–40 used

# pts	$\alpha_{2,1}^{(n)}$	$\beta_{2,1}^{(n)}$
100	0.693905 ± 0.024272	1.150159 ± 0.076637
250	0.708339 ± 0.011373	1.169491 ± 0.035910
500	0.703530 ± 0.014324	1.221910 ± 0.045228
750	0.727740 ± 0.016855	1.165622 ± 0.053221
1,000	0.732002 ± 0.014138	1.165663 ± 0.044642
2,000	0.752371 ± 0.016913	1.131156 ± 0.053402
2,500	0.762282 ± 0.012706	1.106974 ± 0.040117
5,000	0.768990 ± 0.015844	1.109482 ± 0.050026
10,000	0.782166 ± 0.015283	1.087864 ± 0.048257
25,000	0.804136 ± 0.015535	1.040560 ± 0.049052
50,000	0.810475 ± 0.014195	1.037841 ± 0.044821
100,000	0.826284 ± 0.014664	0.998123 ± 0.046302
250,000	0.841989 ± 0.015627	0.963708 ± 0.049343
500,000	0.851244 ± 0.015557	0.945327 ± 0.049121

- [3] Rayna Andreeva, Katharina Limbeck, Bastian Rieck, and Rik Sarkar. Metric space magnitude and generalisation in neural networks. In *Proceedings of 2nd Annual Workshop on Topology, Algebra, and Geometry in Machine Learning (TAG-ML)*, volume 221 of *Proceedings of Machine Learning Research*, pages 242–253. PMLR, 28 Jul 2023. 1
- [4] James AD Binnie, Paweł Dłotko, John Harvey, Jakub Malinowski, and Ka Man Yim. A survey of dimension estimation methods. *arXiv preprint arXiv:2507.13887*, 2025. 1, 5, 6, 8
- [5] Tolga Birdal, Aaron Lou, Leonidas Guibas, and Umut Şimşekli. Intrinsic dimension, persistent homology and generalization in neural networks. In *Proceedings of the 35th International Conference on Neural Information Processing Systems, NIPS '21*, 2021. 1, 6
- [6] Omer Bobrowski and Primoz Skraba. A universal null-distribution for topological data analysis. *Scientific reports*, 13(1):12274, 2023. 1
- [7] Omer Bobrowski and Primoz Skraba. Universality in random persistent homology and scale-invariant functionals. *arXiv preprint arXiv:2406.05553*, 2024. 1, 3

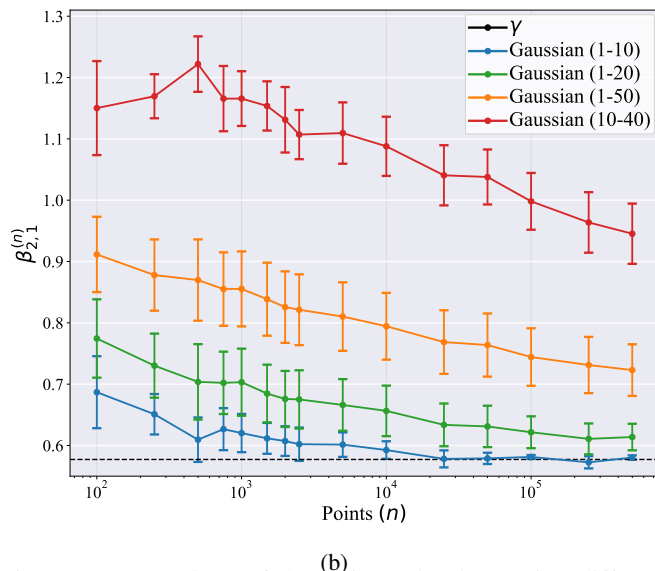
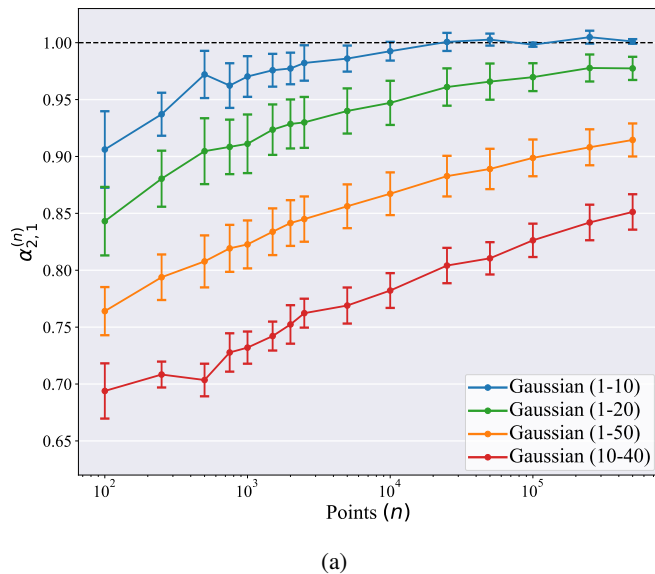


Fig. 7: A comparison of the estimated values using different dimensionality ranges for (a)  $\alpha_{2,1}^{(n)}$  and (b)  $\beta_{2,1}^{(n)}$  for different numbers of points  $n$  sampling from a  $d$ -dimensional Gaussian distribution. The dotted black line indicates the theoretical limit value. The error bars represent the standard deviation.

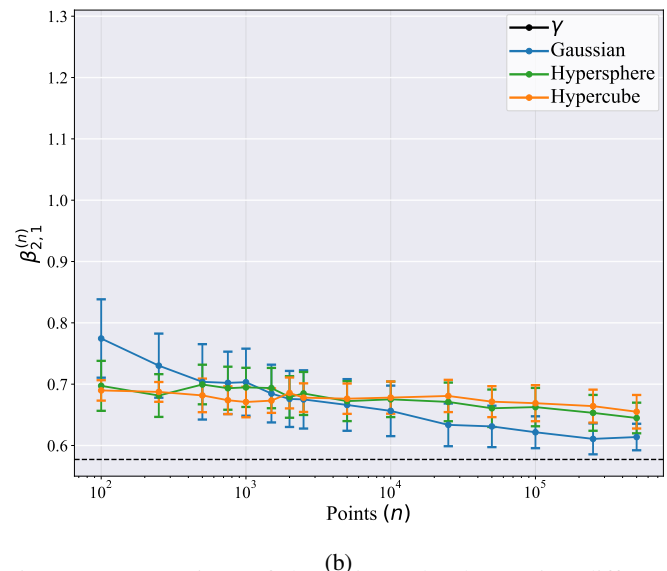
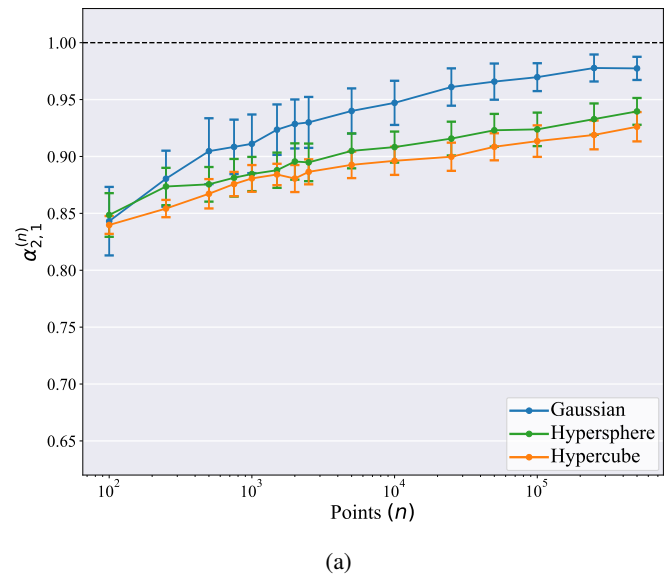


Fig. 8: A comparison of the estimated values using different sampling distributions (a)  $\alpha_{2,1}^{(n)}$  and (b)  $\beta_{2,1}^{(n)}$  for different numbers of points  $n$  using dimensions up to  $d = 20$ . The distributions shown are a  $d$ -dimensional Gaussian distribution, and uniform distributions on a  $d$ -dimensional hypercube and hypersphere. The dotted black line indicates the theoretical limit values. The error bars represent the standard deviation.

[8] G Bouligand. Sur la notion d'ordre de mesure d'un ensemble plan. *Bull. Sci. Math*, 2:185–192, 1929. 1

[9] P. Campadelli, E. Casiraghi, C. Ceruti, and A. Rozza. Intrinsic dimension estimation: Relevant techniques and a benchmark framework. *Mathematical Problems in Engineering*, 2015(1):759567, 2015. 1, 5

[10] Kevin M Carter, Raviv Raich, and Alfred O Hero III. On local intrinsic dimension estimation and its applications. *IEEE Transactions on Signal Processing*, 58(2):650–663, 2009. 1

[11] Claudio Ceruti, Simone Bassis, Alessandro Rozza, Gabriele Lombardi, Elena Casiraghi, and Paola Campadelli. DANCo: An intrinsic dimensionality estimator exploiting angle and norm concentration. *Pattern recognition*, 47(8):2569–2581, 2014. 1, 6

[12] Ronald R Coifman and Stéphane Lafon. Diffusion maps. *Applied and computational harmonic analysis*, 21(1):5–30, 2006. 1

[13] Ron Cole and Mark Fanty. ISOLET. UCI Machine Learning Repository, 1991. DOI: <https://doi.org/10.24432/C51G69>. 5

[14] J.A. Costa and A.O. Hero. Entropic graphs for manifold learning. In *The Thirty-Seventh Asilomar Conference on Signals, Systems and Computers, 2003*, volume 1, pages 316–320, 2003. 6

[15] Jose A Costa and Alfred O Hero. Geodesic entropic graphs for dimension and entropy estimation in manifold learning. *IEEE Transactions on Signal Processing*, 52(8):2210–2221, 2004. 1

[16] Jose A. Costa and Alfred O. Hero. Learning intrinsic dimension and intrinsic entropy of high-dimensional datasets. In *2004 12th European Signal Processing Conference*, pages 369–372, 2004. 1

[17] Francesco Denti, Diego Doimo, Alessandro Laio, and Antonietta Mira. The generalized ratios intrinsic dimension estimator. *Scientific Reports*, 12:20005, 11 2022. 1, 5, 6

[18] Elena Facco, Maria d'Errico, Alex Rodriguez, and Alessandro Laio. Estimating the intrinsic dimension of datasets by a minimal neighborhood information. *Scientific Reports*, 7, 09 2017. 1, 5, 6

[19] Mingyu Fan, Nannan Gu, Hong Qiao, and Bo Zhang. Intrinsic dimension estimation of data by principal component analysis. *arXiv preprint arXiv:1002.2050*, 2010. 1, 6

[20] Jevgenij Gamper and Nasir Rajpoot. Multiple instance captioning: Learning representations from histopathology textbooks and articles.

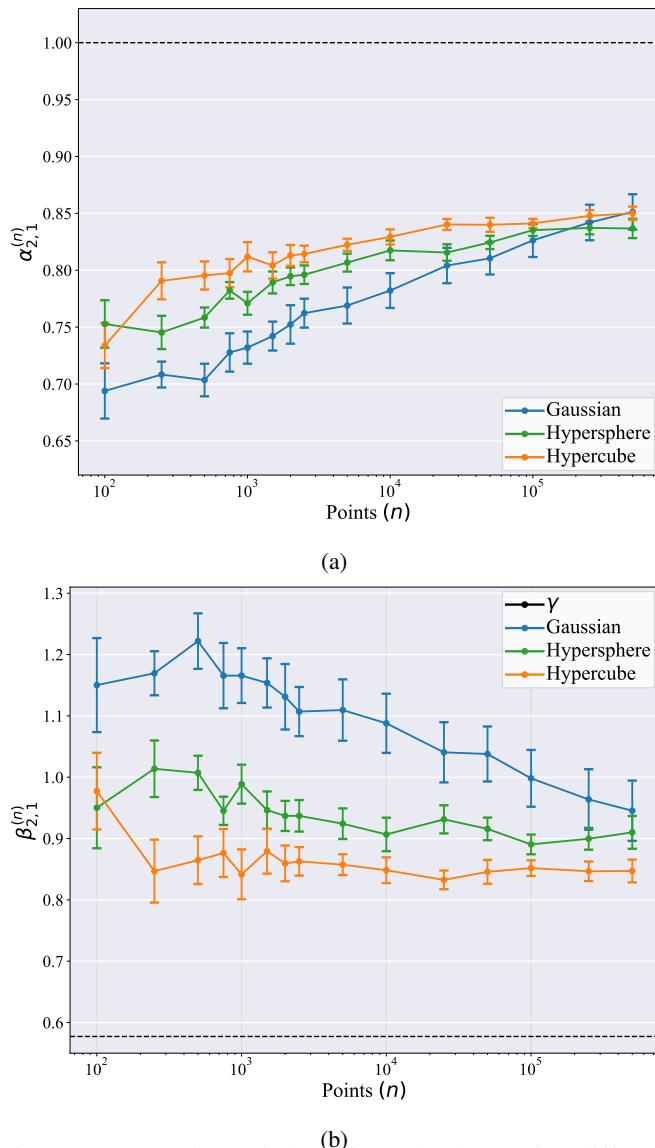


Fig. 9: A comparison of the estimated values using different sampling distributions (a)  $\alpha_{2,1}^{(n)}$  and (b)  $\beta_{2,1}^{(n)}$  for different numbers of points  $n$  using samples from dimensions 10–40. The distributions shown are a  $d$ -dimensional Gaussian distribution, and uniform distributions on a  $d$ -dimensional hypercube and hypersphere. The dotted black line indicates the theoretical limit values. The error bars represent the standard deviation.

In *Proceedings of the IEEE/CVF conference on computer vision and pattern recognition*, pages 16549–16559, 2021. 1

- [21] Sixue Gong, Vishnu Naresh Boddeti, and Anil K Jain. On the intrinsic dimensionality of image representations. In *Proceedings of the IEEE/CVF Conference on Computer Vision and Pattern Recognition*, pages 3987–3996, 2019. 1
- [22] Peter Grassberger and Itamar Procaccia. Characterization of strange attractors. *Physical review letters*, 50(5):346, 1983. 1, 6
- [23] Christian Horvat and Jean-Pascal Pfister. Intrinsic dimensionality estimation using normalizing flows. In *Advances in Neural Information Processing Systems*, volume 35, pages 12225–12236, 2022. 1
- [24] Kerstin Johnsson, Charlotte Sonesson, and Magnus Fontes. Low bias local intrinsic dimension estimation from expected simplex skewness. *IEEE Transactions on Pattern Analysis and Machine Intelligence*, 37(1):196–202, 2015. 6

- [25] Matthäus Kleindessner and Ulrike Luxburg. Dimensionality estimation without distances. In *Proceedings of the Eighteenth International Conference on Artificial Intelligence and Statistics*, volume 38 of *Proceedings of Machine Learning Research*, pages 471–479. PMLR, 2015. 6
- [26] Alex Krizhevsky and Geoffrey Hinton. Learning multiple layers of features from tiny images. Technical Report 0, University of Toronto, Toronto, Ontario, 2009. 5
- [27] Tommi Kärkkäinen and Jan Hänninen. Additive autoencoder for dimension estimation. *Neurocomputing*, 551:126520, 2023. 1
- [28] Y. LeCun, L. Bottou, Y. Bengio, and P. Haffner. Gradient-based learning applied to document recognition. *Proceedings of the IEEE*, 86(11):2278–2324, 1998. 5
- [29] Elizaveta Levina and Peter J. Bickel. Maximum likelihood estimation of intrinsic dimension. In *Proceedings of the 18th International Conference on Neural Information Processing Systems, NIPS’04*, page 777–784, 2004. 1, 3, 6
- [30] Anna V Little, Jason Lee, Yoon-Mo Jung, and Mauro Maggioni. Estimation of intrinsic dimensionality of samples from noisy low-dimensional manifolds in high dimensions with multiscale SVD. In *2009 IEEE/SP 15th Workshop on Statistical Signal Processing*, pages 85–88. IEEE, 2009. 1
- [31] Gabriele Lombardi, Alessandro Rozza, Claudio Ceruti, Elena Casiraghi, and Paola Campadelli. Minimum neighbor distance estimators of intrinsic dimension. In Dimitrios Gunopulos, Thomas Hofmann, Donato Malerba, and Michalis Vazirgiannis, editors, *Machine Learning and Knowledge Discovery in Databases*, pages 374–389, 2011. 6
- [32] Peter Lorenz, Ricard L Durall, and Janis Keuper. Detecting images generated by deep diffusion models using their local intrinsic dimensionality. In *Proceedings of the IEEE/CVF International Conference on Computer Vision*, pages 448–459, 2023. 1
- [33] CW Lung and ZQ Mu. Fractal dimension measured with perimeter-area relation and toughness of materials. *Physical Review B*, 38(16):11781, 1988. 1
- [34] Mathew Penrose. *Random geometric graphs*, volume 5. OUP Oxford, 2003. 4
- [35] Mathew D. Penrose and Joseph E. Yukich. Limit theory for point processes in manifolds. *Annals of Applied Probability*, 23:2161–2211, 2013. 3, 4, 8
- [36] Phil Pope, Chen Zhu, Ahmed Abdelkader, Micah Goldblum, and Tom Goldstein. The intrinsic dimension of images and its impact on learning. In *International Conference on Learning Representations*, 2021. 1
- [37] Haiquan Qiu, Youlong Yang, and Hua Pan. Underestimation modification for intrinsic dimension estimation. *Pattern Recognition*, 140:109580, 2023. 1
- [38] J.W. Sammon. A nonlinear mapping for data structure analysis. *IEEE Transactions on Computers*, C-18(5):401–409, 1969. 1
- [39] Floris Takens. On the numerical determination of the dimension of an attractor. *Lect. Notes in Mathematics*, 898:366–381, 1981. 1
- [40] Piotr Tempczyk, Rafał Michaluk, Lukasz Garncarek, Przemysław Spurek, Jacek Tabor, and Adam Golinski. Lidl: Local intrinsic dimension estimation using approximate likelihood. In *International Conference on Machine Learning*, pages 21205–21231. PMLR, 2022. 1
- [41] Joshua B. Tenenbaum, Vin de Silva, and John C. Langford. A global geometric framework for nonlinear dimensionality reduction. *Science*, 290(5500):2319–2323, 2000. 1, 5
- [42] Nick Whiteley, Annie Gray, and Patrick Rubin-Delanchy. Statistical exploration of the manifold hypothesis. *Journal of the Royal Statistical Society: Series B*, 2025. 1
- [43] Xin Yang, Sebastien Mischea, and Hongyuan Zha. Conical dimension as an intrinsic dimension estimator and its applications. In *Proceedings of the 2007 SIAM International Conference on Data Mining*, pages 169–179. SIAM, 2007. 6
- [44] Shuo Zhou, Antoinette Tordesillas, Mehdi Pouragha, James Bailey, and Howard Bondell. On local intrinsic dimensionality of deformation in complex materials. *Scientific reports*, 11(1):10216, 2021. 1